The Atacama Cosmology Telescope CMB Lensing from Daytime Data: A First Demonstration

Irene Abril-Cabezas[©], ^{1, 2, *} Frank J. Qu[©], ^{3, 4} Joshua Kim[©], ⁵ Mathew S. Madhavacheril[©], ⁵ Karen

```
Perez-Sarmiento<sup>®</sup>, Zachary Atkins<sup>®</sup>, Erminia Calabrese, Anthony Challinor<sup>®</sup>, 2, 1 Mark J. Devlin <sup>®</sup>, 5
  Adriaan J. Duivenvoorden<sup>©</sup>, Jo Dunkley<sup>©</sup>, <sup>6, 10</sup> Alexander van Engelen, <sup>11</sup> Simone Ferraro <sup>©</sup>, <sup>12, 13</sup> Emily
  Finson, <sup>14</sup> Carlos Hervías-Caimapo<sup>©</sup>, <sup>15</sup> Matt Hilton<sup>©</sup>, <sup>16, 17</sup> Arthur Kosowsky<sup>©</sup>, <sup>18</sup> Aleksandra Kusiak<sup>©</sup>, <sup>8, 2</sup>
 Thibaut Louis<sup>©</sup>, <sup>19</sup> Niall MacCrann<sup>©</sup>, <sup>1, 2</sup> Kavilan Moodley<sup>©</sup>, <sup>17</sup> Toshiya Namikawa<sup>©</sup>, <sup>20, 1, 2</sup> Sigurd Næss<sup>©</sup>, <sup>21</sup>
  Lyman A. Page,<sup>6</sup> Adrien La Posta<sup>©</sup>,<sup>22</sup> Emmanuel Schaan<sup>©</sup>,<sup>3,4</sup> Neelima Sehgal<sup>©</sup>,<sup>14</sup> Blake D. Sherwin,<sup>1,2</sup>
Carlos E. Sierra, 3,4 Cristóbal Sifón, 23 Suzanne T. Staggs, Emilie Storer, 24,6 and Edward J. Wollack, 25
                                                     (ACT Collaboration)
<sup>1</sup>DAMTP, Centre for Mathematical Sciences, University of Cambridge, Wilberforce Road, Cambridge CB3 OWA, UK
                <sup>2</sup>Kavli Institute for Cosmology Cambridge, Madingley Road, Cambridge, CB3 0HA, UK
                                 <sup>3</sup>Kavli Institute for Particle Astrophysics and Cosmology,
                                  382 Via Pueblo Mall, Stanford, CA 94305-4060, USA
             <sup>4</sup>SLAC National Accelerator Laboratory, 2575 Sand Hill Road, Menlo Park, CA 94025, USA
                          <sup>5</sup>Department of Physics and Astronomy, University of Pennsylvania,
                                   209 South 33rd Street, Philadelphia, PA 19104, USA
                                   <sup>6</sup>Joseph Henry Laboratories of Physics, Jadwin Hall,
                                     Princeton University, Princeton, NJ 08544, USA
         <sup>7</sup>School of Physics and Astronomy, Cardiff University, The Parade, Cardiff, Wales CF24 3AA, UK
                          <sup>8</sup>Institute of Astronomy, Madingley Road, Cambridge CB3 0HA, UK
              <sup>9</sup> Max-Planck-Institut fur Astrophysik, Karl-Schwarzschild-Str. 1, 85748 Garching, Germany
                                   <sup>10</sup>Department of Astrophysical Sciences, Peyton Hall,
                                     Princeton University, Princeton, NJ 08544, USA
             <sup>11</sup>School of Earth and Space Exploration, Arizona State University, Tempe, AZ 85287, USA
              <sup>12</sup>Lawrence Berkeley National Laboratory, One Cyclotron Road, Berkeley, CA 94720, USA
                           <sup>13</sup>Berkeley Center for Cosmological Physics, Department of Physics,
                                    University of California, Berkeley, CA 94720, USA
            <sup>14</sup>Physics and Astronomy Department, Stony Brook University, Stony Brook, NY 11794, USA
                                 <sup>15</sup>Instituto de Astrofísica and Centro de Astro-Ingeniería,
                               Facultad de Física, Pontificia Universidad Católica de Chile,
                                    Vicuña Mackenna 4860, 7820436 Macul, Santiago, Chile
                                     <sup>16</sup> Wits Centre for Astrophysics, School of Physics,
                   University of the Witwatersrand, Private Bag 3, 2050, Johannesburg, South Africa
              <sup>17</sup> Astrophysics Research Centre, School of Mathematics, Statistics, and Computer Science,
                      University of KwaZulu-Natal, Westville Campus, Durban 4041, South Africa
            <sup>18</sup>Department of Physics and Astronomy, University of Pittsburgh, Pittsburgh, PA 15260, USA
                         <sup>19</sup> Université Paris-Saclay, CNRS/IN2P3, IJCLab, 91405 Orsay, France
                                 <sup>20</sup>Center for Data-Driven Discovery, Kavli IPMU (WPI),
                               UTIAS, The University of Tokyo, Kashiwa, 277-8583, Japan
                           <sup>21</sup>Institute of Theoretical Astrophysics, University of Oslo, Norway
                  <sup>22</sup>Department of Physics, University of Oxford, Keble Road, Oxford, OX1 3RH, UK
         <sup>23</sup>Instituto de Física, Pontificia Universidad Católica de Valparaíso, Casilla 4059, Valparaíso, Chile
                      <sup>24</sup>Physics Department, McGill University, Montreal, QC H3A 0G4, Canada
               <sup>25</sup>NASA Goddard Space Flight Center, 8800 Greenbelt Road, Greenbelt, MD 20771, USA
                                                  (Dated: November 14, 2025)
```

We present a cosmic microwave background (CMB) lensing power spectrum analysis using daytime data (11am–11pm UTC) gathered by the Atacama Cosmology Telescope (ACT) over the period 2017–2022 (ACT Data Release 6). This dataset is challenging to analyze because the Sun heats and deforms the telescope mirror, complicating the characterization of the telescope. We perform more than one hundred null and consistency checks to ensure the robustness of our measurement and its compatibility with nighttime observations. We detect the CMB lensing power spectrum at 17σ significance, with an amplitude $A_{\rm lens}=1.045\pm0.063$ with respect to the prediction from the best-fit Planck-ACT CMB power spectrum Λ CDM cosmology. In combination with the Dark Energy Spectroscopic Instrument (DESI) Baryon Acoustic Oscillation (BAO) data, this corresponds to a constraint on the amplitude of matter fluctuations $\sigma_8=0.826\pm0.027$. The analysis presented here is especially relevant for ground-based millimeter-wave CMB experiments, paving the way for future analyses making use of both nighttime and daytime data to place tight constraints on cosmological parameters.

Introduction—As photons from the cosmic microwave background (CMB) travel to us, they encounter large-scale structure that gravitationally deflects their trajectories. This phenomenon is known as weak gravitational lensing of the CMB, and it has emerged as a robust and powerful observable for precision cosmology (for a review, see, e.g., [1]). Reference [2] presented the first joint analysis of the CMB lensing power spectrum with data from multiple telescopes, namely the Atacama Cosmology Telescope (ACT) [3–5], Planck [6] and the South Pole Telescope (SPT) [7]. It provided the most precise CMB lensing power spectrum measurement to date (with a signal-to-noise ratio SNR of 61), which can be used to probe the growth of structure and place tight constraints on neutrino mass [8, 9] or primordial non-Gaussianity (in cross-correlation with another biased tracer) [10, 11].

The ACT Data Release 6 (DR6) lensing analysis [3–5] utilized data taken during the night only. However, half of the time-ordered-data (TOD)¹ collected by ACT was during the day (between 11am and 11pm UTC). This work focuses on the corresponding CMB lensing power spectrum analysis using daytime data only. Working with daytime data is challenging because the Sun heats and deforms the telescope structure and mirrors, making it difficult to characterize the beam profile [14].² We find two intuitive reasons why a measurement of CMB lensing could be robust against ACT daytime complexities. Firstly, the time variation of the telescope beam on timescales of hours, which could lead to a smoothly varying position-dependent beam, would mostly affect the reconstruction of the largest-scale CMB lenses (which are already excluded from our analysis, see [3]). Secondly, beam mis-modeling would not produce the exact same effect on the CMB power spectrum as the squeezing and stretching due to real lensing, meaning that these two effects are not fully degenerate. With these arguments in mind, it is a promising avenue to utilize daytime data to increase the signal-to-noise of the current state-ofthe-art ACT nighttime-only lensing measurement (43σ) significance [3]).³ This is one of the improvements anticipated for the final ACT analysis, which we denote ACT DR6+ [17-19].

Data collection—The final ACT DR6 dataset [13] was

collected during the period 2017–2022. Until mid-2019, the daytime observations concentrated on two small regions, which we refer to as daydeep. They cover approximately 8% of the sky with a median depth of 9 μ K-arcmin (see top panel of Fig. 1). Thereafter, the daytime scanning strategy followed that of night. We refer to the corresponding observations as daywide. They cover almost half the sky with a median depth of 27 μ K-arcmin (see bottom panel of Fig. 1).

In this analysis, we only use data at 90 GHz and 150 GHz, which were gathered by ACT polarized arrays (PA) 5 and 6 [13, 20]. This choice is motivated by the systematics and null tests carried out in previous ACT power spectrum and lensing analyses [3, 21], which validated the corresponding nighttime data gathered by those polarized arrays, together with foreground contamination studies [5, 22]. In addition, we only analyse PA5 data for daywide; the PA6 dataset is too shallow because it was replaced with a low-frequency array (30 GHz and 40 GHz) soon after the daywide survey started.

Data selection and noise modeling—Our starting point is the ACT DR6 source-free maps.⁶ Prior to the final making of those maps, various data cuts and corrections are applied (e.g., removing data samples with the Sun or Moon in the far sidelobes, or with high beam variability), described in more detail in [13, 14]. We further remove areas with poor cross-linking [12] or with root-meansquare (RMS) map noise larger than 70 µK-arcmin. Areas at the edge of the map with high noise are also removed after careful visual inspection. We further exclude regions of bright Galactic emission following the same approach as [3], primarily by intersecting the ACT footprint with the *Planck* 70% Galactic mask. We use the common resulting area within daydeep or daywide (shown with gray lines in Fig. 1) to generate map-based noise models using the MNMS approach [12], and draw noise simulations from these.

For daydeep, we further shrink the daydeep mask by 1.5° around the perimeter to mitigate any edge effects. Preliminary null tests informed our decision to remove the left half of the southern daydeep patch,

^{*} ia404@cam.ac.uk

¹ A TOD is a data unit, typically 11 minutes long [13, 15, 16].

² It also leads to pointing offsets, although the new per-TOD pointing corrections used in the DR6 pipeline successfully correct for them [13].

³ We note that the latest ACT-only lensing analysis [3–5] was based on nighttime observations using the dr6.01 map version. Since then, we have made refinements to the map-making that improve the large-scale transfer function and polarization noise levels. This work uses daytime observations from the dr6.02 re-processing of the ACT DR6 dataset that includes these improvements (ACT DR6 public data release).

⁴ These maps are labeled as act_dr6.02_std_DN_day, act_dr6.02_std_DS_day in the public ACT DR6 release. Details on data access are available in the *Data Availability* section at the end of this work.

⁵ These maps are labeled as act_dr6.02_std_AA_day in the public ACT DR6 release.

 $^{^6}$ These maps are labeled as ${\tt map_srcfree}$ in the public ACT DR6 release.

⁷ HFI_Mask_GalPlane-apo0_2048_R2.00.fits, available on the Planck Legacy Archive (https://pla.esac.esa.int/). The 70% mask retains the 70% of the sky with the lowest dust contamination and has been validated to have a negligible impact on the inferred CMB lensing power spectrum amplitude for an ACT-like survey [22].

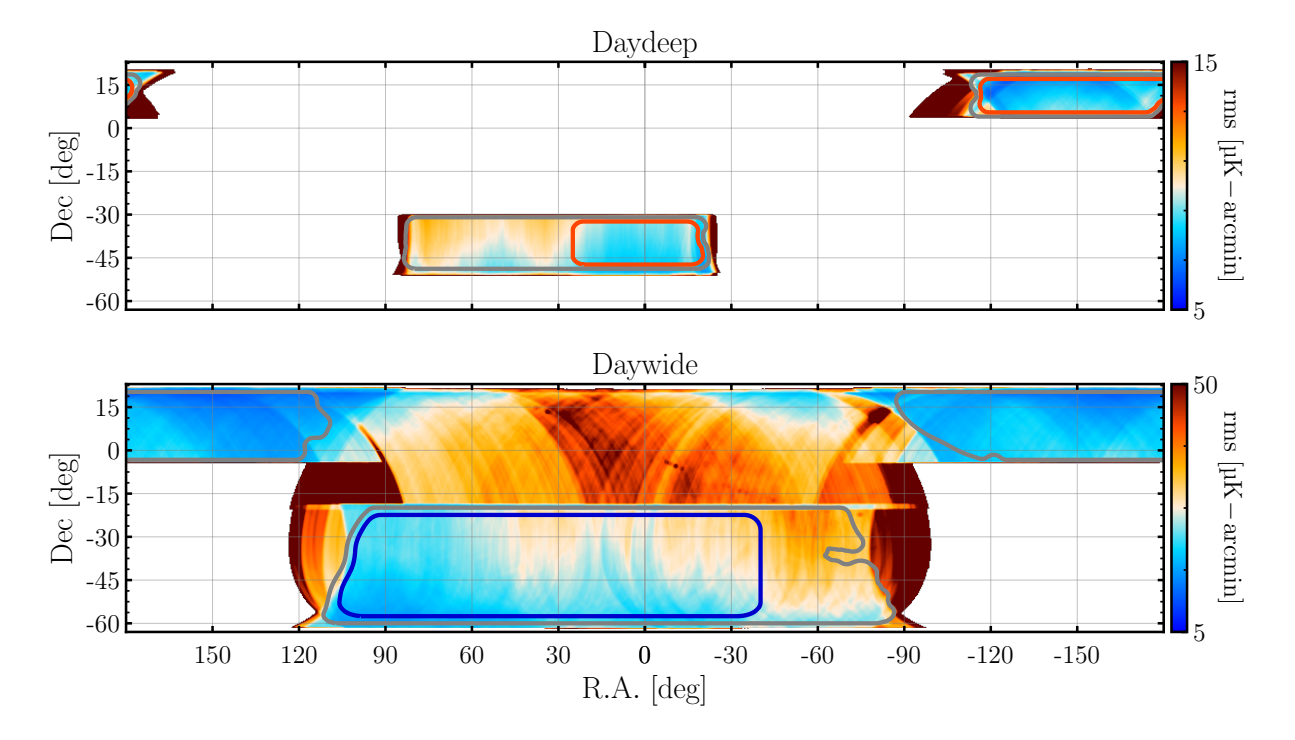


FIG. 1. Map of root-mean-square (RMS) noise per pixel for daydeep (top) and daywide (bottom) derived from inverse-variance maps (that describe the noise behavior on small scales [12, 13]). Regions such as the left half of the southern daydeep patch are shallower due to data cuts prior to map-making, such as beam cuts (summarized in the beam-badness statistic; see [13, 14]). The RMS maps, together with cross-linking and Galactic dust emission information, inform the choice of area that we model and simulate (encircled with gray contours). Further null tests inform the regions we use in our lensing power spectrum analysis: daywide South, shown in blue, with a mean depth of $24\,\mu\text{K}$ -arcmin and effective sky fraction $f_{\text{sky}} = 0.08$; and daydeep, shown in orange, with a mean depth of $8\,\mu\text{K}$ -arcmin and $f_{\text{sky}} = 0.02$.

which already had shallower coverage due to beam-informed observation cuts (summarized in the beam-badness statistic; see [13, 14]).⁸ The corresponding effective sky fraction of daydeep after apodizing the masks on 3° scales is $f_{\rm sky}=2\%$. This is shown in orange in the top panel of Fig. 1. For daywide, we shrink the daywide mask by 2.5° and exclude high variance regions when we perform the lensing reconstruction. The final mask is apodized on 3° scales. In the end, we are forced to exclude completely the daywide North region from our analysis as it fails multiple null tests.⁹ The final daywide mask is marked in blue in the bottom panel of Fig. 1 ($f_{\rm sky}=8\%$).

Data pre-processing and calibration—Before the source-free maps pass through the lensing reconstruction

pipeline,¹⁰ we process them following the approach described in detail in [3]. In summary, this involves first downgrading the maps to a pixel resolution of 1 arcmin. Then, we inpaint regions around residual compact-object sources in our maps [3, 23] by smoothly interpolating from surrounding values and further adding white noise based on the map inverse variance. The emission from tSZ-selected clusters is estimated and subtracted, for which we use the NEMO¹¹ software [24]. We also deconvolve the pixel window function introduced by the downgrading operation and mask Fourier modes with $|\ell_x| < 90$ and $|\ell_y| < 50$ to remove ground pickup, following [21]. Finally, we beam-deconvolve each daytime map [25].

The daytime beams are estimated in [13, 25] using both the profile of point sources in the daytime maps (which informs the small-scale behavior) and the relative CMB power spectrum between night and day maps for each array-band.¹² The beam derived from the CMB power spectrum comparison is valid for $\ell \lesssim 4000$, but

⁸ As noted in Section 5.2., pp 186-188 [14], it was noticed during the ACT DR4 daytime work that the beams showed the most pathological behavior in the ACT DR4 South patch (roughly corresponding to the ACT DR6 daydeep southern region); however, an understanding of the physical mechanism was not identified.

⁹ These failures were not surprising to us since we found a two-point power-spectrum mismatch between the corresponding night and daywide array-bands, especially at multipoles $\ell_{\rm CMB} < 1000$.

 $^{^{10}}$ https://github.com/simonsobs/so-lenspipe

¹¹ https://nemo-sz.readthedocs.io/

¹² When this ratio is too noisy, both night and day spectra

TABLE I. We find that daytime data can be made reliable for lensing with a suitable process of rescaling to nighttime data. We therefore apply an additional calibration factor (fourth column), which we treat as a gain, in the pre-processing of these maps. This factor is obtained by comparing each array-band daytime temperature power spectrum to the corresponding array-band power spectrum of nighttime observations, within the multipole range $1000 < \ell < 2000$.

Daytime	Array	Band [GHz]	Calibration
day deep	PA5	90	1.0459
day deep	PA5	150	0.9746
day deep	PA6	90	1.0231
day deep	PA6	150	0.9281
daywide	PA5	90	1.0437
daywide	PA5	150	0.9777

has relatively large error bars throughout. The point source beam has much higher SNR but is only valid for $\ell > 2000$ due to low-pass filtering in its production. The point source beam is estimated from stacking all point sources within $10 \times 20 \text{ deg}^2$ tiles, which are then averaged to a common beam across all tiles using inversevariance weighting. It has an unknown normalization because almost all the bright point sources are strongly variable. We merge these two beam measurements by fitting a relative normalization for the point source beam in their overlapping multipole range and fitting a smooth function¹³ to the normalized beams. The procedure results in an effective beam that also takes into account both the transfer function at low ℓ in total intensity and the absolute gain calibration to be applied to each arrayband. Unfortunately, the dataset lacks the sensitivity to estimate the effective beam for polarization, which should not include a transfer function [13, 26] and might further need a polarization efficiency correction. Therefore, since these beams are approximate and may not be accurate at low multipoles, ¹⁴ we run specific tests to ensure that our results are robust to the choice of minimum multipole

are calibrated with respect to *Planck* first via their autoand cross-spectra. Using *Planck* as a noise-reducing template only introduces sensitivity to *Planck*'s phases (but not to its amplitude).

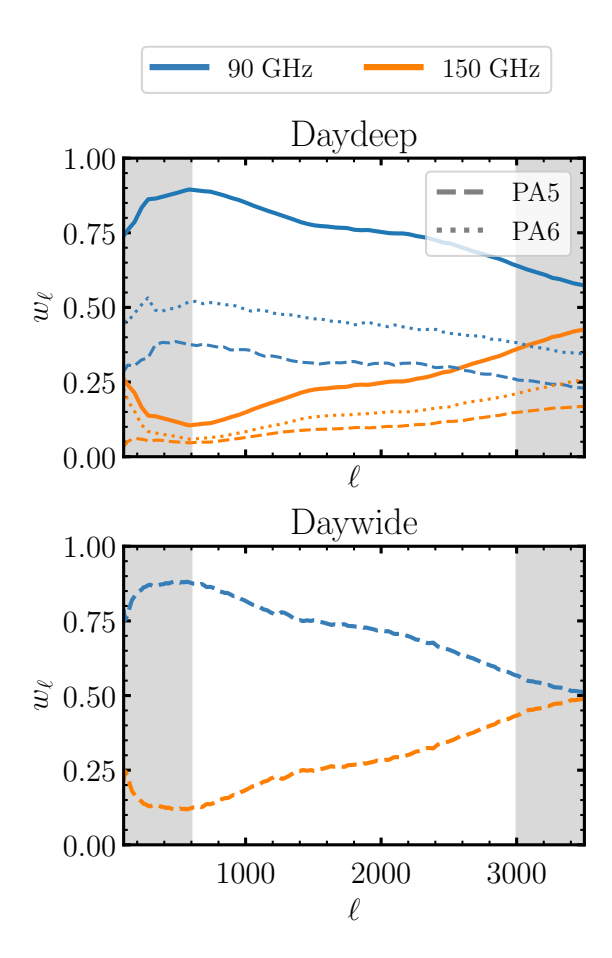


FIG. 2. Maps from detector array-bands (PA) are combined using inverse-variance weights in harmonic space to form coadded daydeep and daywide sky maps, following the same approach as [3]. This figure shows the weights w_{ℓ} applied to each array-band map as a function of multipole. They sum to unity at each multipole to preserve the CMB signal. For daydeep, the total weights assigned to each frequency are shown with solid lines. We shade in gray the CMB scales excluded in our analysis (for which we only include $600 < \ell_{\rm CMB} < 3000$, informed by foreground contamination studies [5, 22]). The PA6 daywide dataset is excluded from our analysis as it is too shallow.

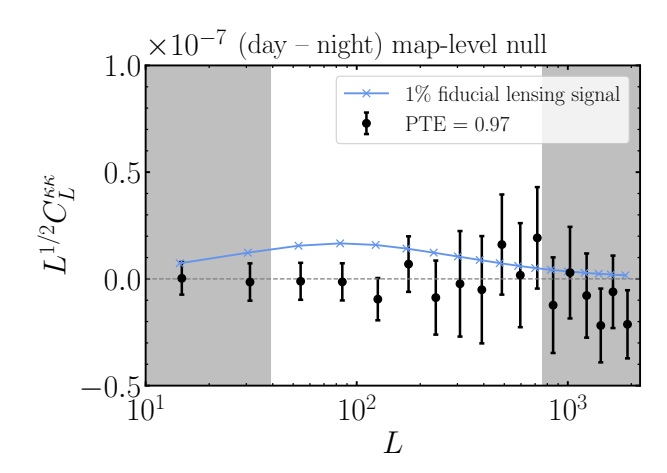
used in the lensing power spectrum reconstruction, and which we describe in more detail in the next section.

After pre-processing the maps as described above, we ensure that the temperature power spectrum for each resulting array-band map is consistent between night and day. We do this by measuring the relative power spectrum of day with respect to night in the range $1000 < \ell < 2000$. We find that this ratio is constant within that range, and treat this factor as a gain calibration. The factors are reported in Table I.

Finally, the different array-bands within each daytime dataset (daydeep, daywide) are combined in harmonic space using inverse-variance weighting following [3], where the noise power spectra are estimated from

¹³ The model consists of a smooth function multiplying the nighttime beam. The smooth function is the product of two sigmoid functions, chosen ad-hoc for its reasonably good fit to the data given its 6 degrees of freedom. The smoothing is necessary to reduce the scatter in what would otherwise be a quite noisy beam model, but the result still falls short of the reliability of the nighttime beam.

The ACT DR6 daytime beams were published with the following caveats: "The beams are only applicable to Stokes I because they include the low-multipole map-making transfer function that is present in the Stokes I maps but not in the polarization maps. The beams should work decently for polarization at multipoles above $\ell \sim 1000$, but users should be careful and check that results are stable with choice of ℓ_{\min} " (LAMBDA ACT (DR6.02) Harmonic Beam Profiles).



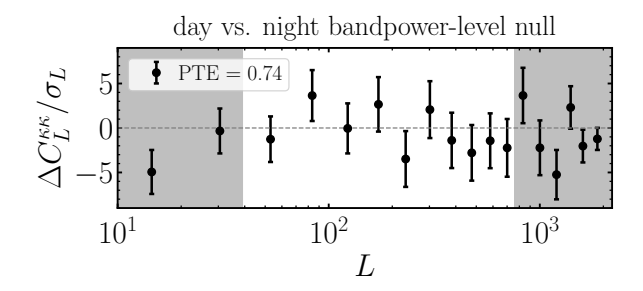


FIG. 3. We validate the ACT DR6 daytime lensing power spectrum with a suite of null tests targeted at potential systematics in the daytime data. Top: The lensing power spectrum reconstructed from the difference between the daytime and nighttime maps. This is a stringent test: the signal is null within 1% of the lensing signal (shown in blue). Bottom: Difference between the lensing power spectrum reconstructed from the daytime data and the ACT dr6.02 nighttime-only lensing power spectra [17], in units of the nighttime-only bandpower errors σ_L . The PTEs for these null tests are calculated from the goodness-of-fit with respect to null, by Monte Carlo sampling from the covariance matrix within the analysis range 40 < L < 763.

the corresponding data splits [3, 12]. The resulting weights are shown in Fig. 2. The contribution from the 150 GHz channels increases with multipole ℓ as the atmospheric noise (which scales with frequency) becomes subdominant.

Measurement validation with null tests—We first perform a suite of null tests to ensure the robustness of our measurement, which we present in more detail in the End Matter. Our analysis followed a blinding policy where no comparisons with theory predictions were allowed until the null tests were passed. Prior to unblinding, we also ensured that none of our null tests lay outside the range 0.001 < PTE < 0.999.

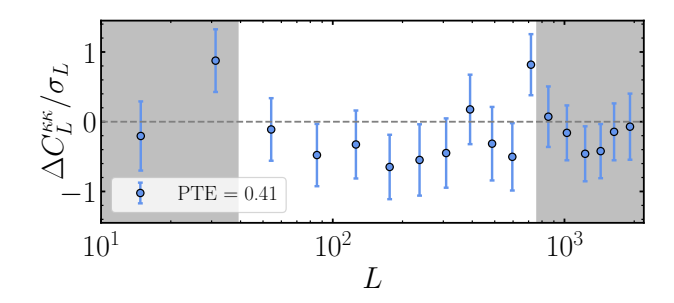


FIG. 4. Difference in the reconstructed lensing bandpowers between our baseline analysis (600 < $\ell_{\rm CMB}$ < 3000) and a reconstruction where only $\ell_{\rm CMB}$ > 1000 modes in polarization are used, divided by the error in the baseline bandpowers σ_L . This test is motivated by the fact that the daytime beams are approximate because the polarization beam includes a transfer function at $\ell_{\rm CMB}$ < 1000 that should only be present in temperature. We find consistency with null, with a PTE of 0.41. Excluding $\ell_{\rm CMB}$ < 1000 modes in polarization minimally affects the sensitivity of our measurement (SNR of 16σ , c.f. baseline is 17σ).

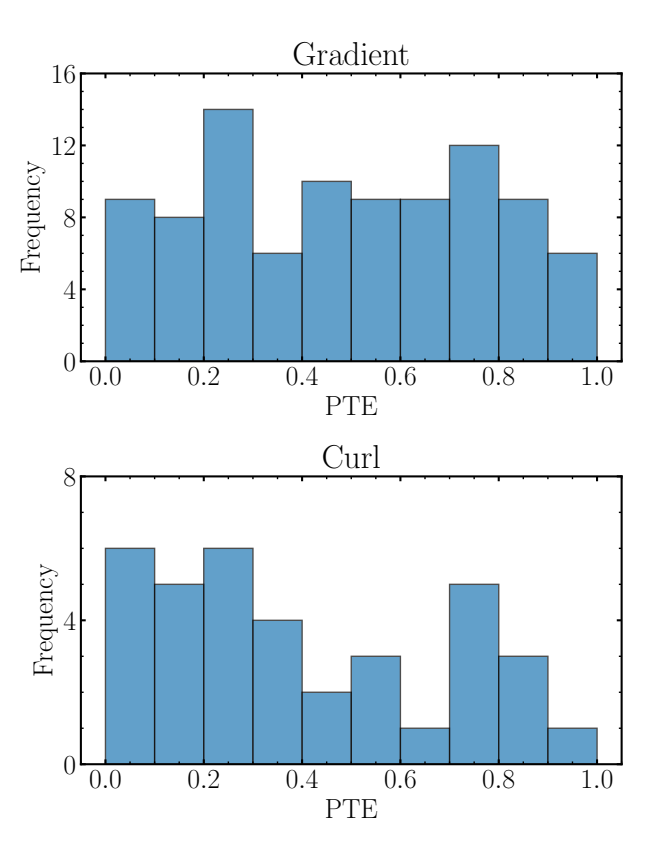


FIG. 5. Histogram of PTE values for all our null tests. The top panel shows the null tests that refer to the measured gradient component of the lensing deflection field, while the bottom panel corresponds to the curl component. Both distributions are consistent with a uniform distribution (Kolmogorov–Smirnov test PTE of 95% and 9%, respectively; with the caveat that this test ignores correlations between the different tests). None of our null tests lie outside the range 0.001 < PTE < 0.999.

¹⁵ The probability to exceed (PTE) is the probability of obtaining a higher χ^2 than what we actually obtain, given a distribution with the same number of degrees of freedom.

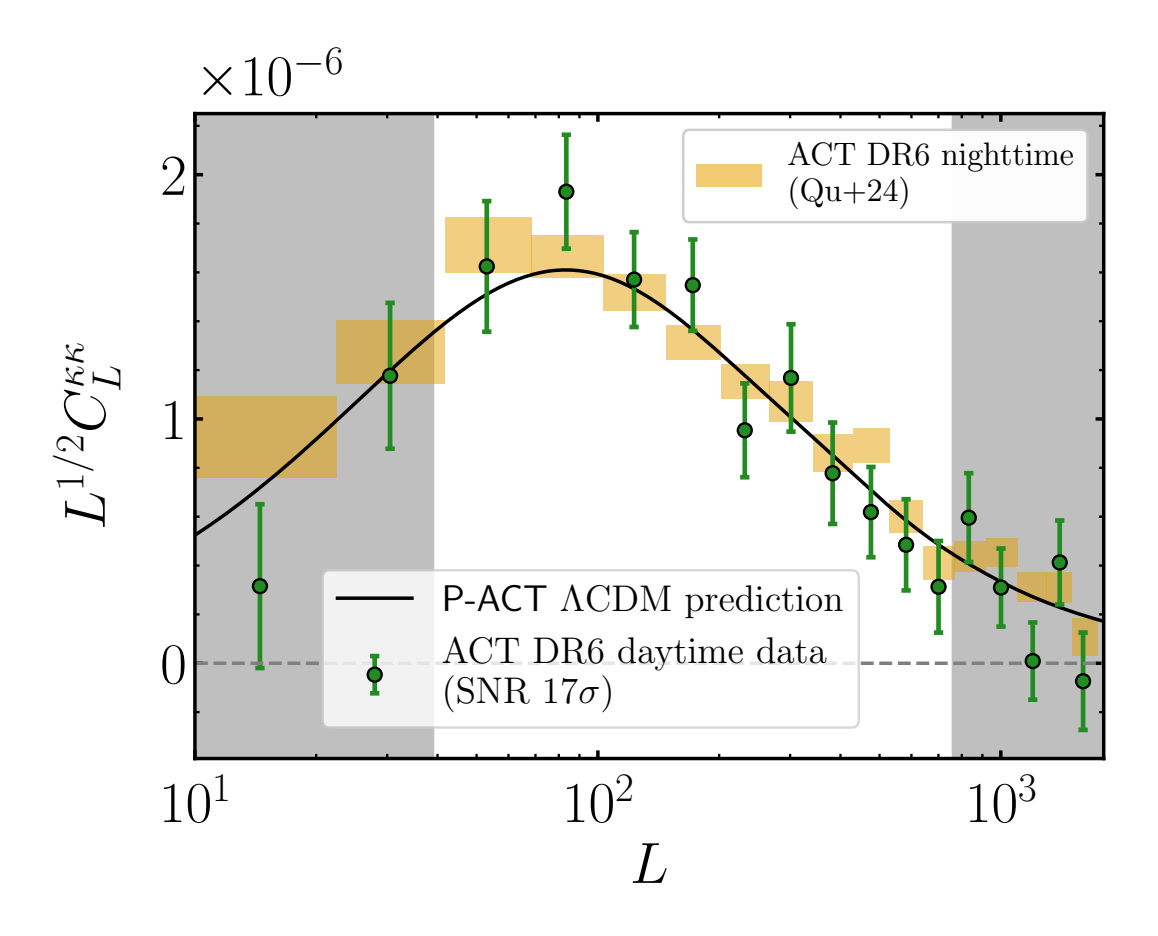


FIG. 6. ACT DR6 daytime lensing potential power spectrum, detected at 17σ within the analysis range 40 < L < 763 (unshaded region; choice verified in [3], see main text for further details). The daytime spectrum results from combining the daydeep and daywide lensing spectra (obtained from both temperature and polarization maps) at the bandpower level. We show in black the Λ CDM prediction from the Planck-ACT (P-ACT) CMB power spectrum [13, 21, 27]. We find a lensing power spectrum amplitude $A_{\rm lens} = 1.045 \pm 0.063$ with respect to this model (PTE of 63%). For reference, we show in boxes the current state-of-the-art ACT lensing analysis with nighttime data (43σ significance [3]).

The null tests are grouped in two categories: map-level and bandpower-level null tests. For each category, we run tests that include all array-bands coadded data, as well as tests that only include a subset of those (PA5, PA6, 90 GHz and 150 GHz-only tests). For map-level null tests, we perform the lensing reconstruction on maps that should contain no signal in the absence of systematic effects. For this, we prepare night vs. day difference maps that are passed into the lensing reconstruction pipeline. We run the reconstructions using the minimumvariance temperature-polarization combination (MV), temperature-only (TT) and polarization-only (MVPol) quadratic estimators (see e.g. [28] for a review on lensing estimators). An example is shown in the top panel of Fig. 3, where we show the lensing reconstruction using the MV estimator on the difference of day and night maps (all frequencies coadded). This is done for both daydeep and daywide data, and the resulting null-test bandpowers are combined using inverse-variance weighting and a covariance derived from simulations. The difference is

consistent with zero at high precision: since map-level nulls remove the CMB signal sample variance, the errors are remarkably small, making them extremely powerful null tests. In some cases, the errors are less than a hundredth of the signal power (for reference we show 1% of the lensing signal in blue in Fig. 3). Therefore, these tests can thus strongly disfavor any additive systematic in the daytime maps that mimics lensing. We quantify the consistency with null by computing the χ^2 with respect to null, which we translate into a PTE value by Monte Carlo sampling from the covariance matrix (PTE of 0.97 for the map-level test presented in Fig. 3). These are presented in Table II (End Matter).

With bandpower-level null tests, we ensure that the lensing spectra using daytime data are consistent with those of night (Table III End Matter; see also bottom panel of Fig. 3). In addition, we ensure internal consistency between our baseline MV reconstruction and those obtained when including less extended ranges of CMB modes (Table III). Variations in the multipole

range test for the impact of foregrounds and the presence of any ground pickup or any additional transfer function. In particular, the polarization beam is approximate, presenting a transfer function at low ℓ that should only be present in temperature. Therefore, we ensure consistency between the bandpowers derived in our baseline analysis and a reconstruction where only $\ell_{\rm CMB} > 1000$ modes in polarization are used. The result is shown in Fig. 4, showing that the difference between both is consistent with null (PTE of 0.41).

Finally, we also check that the curl of the reconstructed deflection field is consistent with zero (Table IV). Only systematic effects could induce a non-zero curl-like signal at these noise levels. Curl null tests are also an excellent test of our simulations and covariance matrices. We summarize the PTE results of all the null tests in Fig. 5. Overall, the PTE distributions corresponding to both the gradient and curl of the lensing deflection field are consistent with uniform (Kolmogorov–Smirnov test PTE of 95% and 9%, respectively; with the caveat that this test ignores correlations between the different tests).

Measurement of the lensing power spectrum—We run the lensing reconstruction for both daydeep and daywide, using the MV estimator with profile hardening [29–32] to mitigate contamination from extragalactic foregrounds. As an example, we show in the End Matter the reconstructed matter density field for the southern region of the daydeep field $(600 \, \text{deg}^2)$. We combine the daydeep and daywide lensing spectra at the power-spectrum level with a covariance derived from simulations. The resulting daytime-only lensing power spectrum $\hat{C}_L^{\kappa\kappa}$ is presented in Fig. 6 and Table V, with a detection significance of 17σ within the analysis range 40 < L < 763. We choose the same multipole range verified in [3, 33] based on null-test stability and foreground estimates [3, 5], and which also minimizes the correlation between bandpowers: 10 bins with non-overlapping bin edges at [40, 66, 101, 145, 199, 264, 339, 426, 526, 638, 763]. The ACT DR6 daytime lensing bandpowers are well fit by a lensing amplitude $A_{\rm lens} = 1.045 \pm 0.063$ relative to the Planck-ACT (P-ACT) [13, 21, 27] ΛCDM prediction (PTE of 63%), which is shown in black in Fig. 6. In combination with Baryon Acoustic Oscillation (BAO) measurements from the Dark Energy Spectroscopic Instrument (DESI DR2) [34, 35], this translates into a constraint on the amplitude of matter fluctuations σ_8 of

 $\sigma_8 = 0.826 \pm 0.027$ (ACT DR6 day + DESI DR2). (1)

This 3.3% measurement on σ_8 is consistent within less than 1σ with the value obtained by ACT DR6 nighttime [4] and by the recent ACT, *Planck* and SPT lensing combination [2]. We present in the End Matter further information on the likelihood and priors used in our analysis, which closely follow previous ones [2–4, 33].

We note that the improvement to the current lensing SNR from the addition of daytime data is underestimated

by naively combining the SNR values of lensing spectra from daytime alone and nighttime alone. The reason for this is that such an estimate neglects the contributions from any day-night cross-terms that would naturally arise when measuring a lensing power spectrum from a day+night coadded map. Fig. 8 (End Matter) presents the per-mode reconstruction noise power for both the daytime and nighttime datasets. We will defer a detailed discussion of the relative contributions of daytime and nighttime data to our final ACT DR6+ lensing papers.

Conclusion—We have presented the first CMB lensing power spectrum analysis using data gathered by the Atacama Cosmology Telescope during the day. We detect the signal at 17σ significance, and validate the resulting lensing power spectrum with a large suite of null tests that target different potential systematic effects in the daytime data and that also ensure consistency with the nighttime bandpowers. We anticipate including this dataset in the upcoming ACT DR6+ lensing analysis [17, 19, 22].

This is a proof of principle demonstration that lensing with daytime data is a possibility, and it is encouraging for future lensing measurements with the Simons Observatory (which is specifically designed to enable full daytime functionality)¹⁶ [36, 37] and the South Pole Telescope (containing a "summer fields" survey extension) [38] in order to place tight constraints on cosmological parameters.

availability—The ACT DR6 Datadataset publicly available on the Legacy Archive for Microwave Background Data Analysis (LAMBDA) https://lambda.gsfc.nasa.gov/product/ act/actadv_prod_table.html and at NERSC at /global/cfs/cdirs/cmb/data/act_dr6/dr6.02. ACT DR6 daytime CMB lensing bandpowers, associated covariance and likelihood can be found at https: //github.com/ACTCollaboration/dr6plus_lenslike and will be made available on LAMBDA.

Acknowledgements—I.A.C. acknowledges support from Fundación Mauricio y Carlota Botton and the Cambridge International Trust. B.D.S. acknowledges support from the European Research Council (ERC) under the European Union's Horizon 2020 research and innovation program (Grant agreement No. 851274). E.C. acknowledges support from the European Research Council (ERC) under the European Union's Horizon 2020 research and innovation programme (Grant agreement No. 849169). A.C. acknowledges support from the STFC (grant numbers ST/W000977/1 and

¹⁶ The main difference with ACT is the use of a carbon fiber backup structure for the mirrors which keeps the mirror panels aligned under different thermal conditions. In addition, the mirrors are housed in a way that minimizes solar radiation further reducing daytime effects.

ST/X006387/1). N.S. acknowledges support from DOE award number DE-SC0025309. C.S. acknowledges support from the Agencia Nacional de Investigación y Desarrollo (ANID) through Basal project FB210003. K.M. acknowledges support from the National Research Foundation of South Africa. M.H. acknowledges support from the National Research Foundation of South Africa (grant numbers 97792, 137975, CPRR240513218388) This work received support from the U.S. Department of Energy under contract number DE-AC02-76SF00515 to SLAC National Accelerator Laboratory.

This research has also made extensive use of TEMPURA¹⁷, FALAFEL¹⁸, SO-LENSPIPE¹⁹, ORPHICS²⁰ and the MNMS [12], ASTROPY [39], NUMPY [40], SCIPY [41] packages. We also acknowledge use of the MATPLOTLIB [42] package to produce the plots in this paper, use of the Boltzmann code CAMB [43] for calculating theory spectra, and use of the GETDIST [44], COBAYA [45] and COSMOSIS [46] software for likelihood analysis and sampling. This work was performed using resources provided by the Cambridge Service for Data Driven Discovery (CSD3) operated by the University of Cambridge Research Computing Service (www.csd3.cam.ac.uk), provided by Dell EMC and Intel using Tier-2 funding from the Engineering and Physical Sciences Research Council (capital grant EP/T022159/1), and DiRAC funding from the Science and Technology Facilities Council (www. dirac.ac.uk). In particular, this work used the DiRAC Data Intensive service. The DiRAC component of CSD3 at Cambridge was funded by BEIS, UKRI and STFC capital funding and STFC operations grants. DiRAC is part of the UKRI Digital Research Infrastructure.

We are grateful to the NASA LAMBDA archive for hosting our data. This work uses products from the Planck satellite, based on observations obtained with Planck (http://www.esa.int/Planck), an ESA science mission with instruments and contributions directly funded by ESA Member States, NASA, and Canada.

Support for ACT was through the U.S. National Science Foundation through awards AST-0408698, AST-0965625, and AST-1440226 for the ACT project, as well as awards PHY-0355328, PHY-0855887 and PHY-1214379. Funding was also provided by Princeton University, the University of Pennsylvania, and a Canada Foundation for Innovation (CFI) award to UBC. ACT operated in the Parque Astronómico Atacama in northern Chile under the auspices of the Agencia Nacional de Investigación y Desarrollo (ANID). The development of multichroic detectors and lenses was supported by NASA grants NNX13AE56G

and NNX14AB58G. Detector research at NIST was supported by the NIST Innovations in Measurement Science program. Computing for ACT was performed using the Princeton Research Computing resources at Princeton University, the National Energy Research Scientific Computing Center (NERSC), and the Niagara supercomputer at the SciNet HPC Consortium. SciNet is funded by the CFI under the auspices of Compute Canada, the Government of Ontario, the Ontario Research Fund–Research Excellence, and the University of Toronto. We thank the Republic of Chile for hosting ACT in the northern Atacama, and the local indigenous Licanantay communities whom we follow in observing and learning from the night sky.

- Lewis, A. & Challinor, A. 2006, astro-ph/0601594, Phys. Rep., 429, 1, Weak gravitational lensing of the CMB
- [2] Qu, F. J., et al. 2025, arXiv:2504.20038, arXiv e-prints, arXiv:2504.20038, Unified and consistent structure growth measurements from joint ACT, SPT and Planck CMB lensing
- [3] Qu, F. J., et al. 2024, arXiv:2304.05202, ApJ, 962, 112, The Atacama Cosmology Telescope: A Measurement of the DR6 CMB Lensing Power Spectrum and Its Implications for Structure Growth
- [4] Madhavacheril, M. S., et al. 2024, arXiv:2304.05203, ApJ, 962, 113, The Atacama Cosmology Telescope: DR6 Gravitational Lensing Map and Cosmological Parameters
- [5] MacCrann, N., et al. 2024, arXiv:2304.05196, ApJ, 966, 138, The Atacama Cosmology Telescope: Mitigating the Impact of Extragalactic Foregrounds for the DR6 Cosmic Microwave Background Lensing Analysis
- [6] Carron, J., Mirmelstein, M., & Lewis, A. 2022, arXiv:2206.07773, J. Cosmology Astropart. Phys., 2022, 039, CMB lensing from Planck PR4 maps
- [7] Ge, F., et al. 2025, arXiv:2411.06000, Phys. Rev. D, 111, 083534, Cosmology from CMB lensing and delensed EE power spectra using 2019–2020 SPT-3G polarization data
- [8] Lesgourgues, J. & Pastor, S. 2006, astro-ph/0603494, Phys. Rep., 429, 307, Massive neutrinos and cosmology
- [9] Allison, R., Caucal, P., Calabrese, E., Dunkley, J., & Louis, T. 2015, arXiv:1509.07471, Phys. Rev. D, 92, 123535, Towards a cosmological neutrino mass detection
- [10] Schmittfull, M. & Seljak, U. 2018, arXiv:1710.09465,
 Phys. Rev. D, 97, 123540, Parameter constraints from cross-correlation of CMB lensing with galaxy clustering
- [11] McCarthy, F., Madhavacheril, M. S., & Maniyar, A. S. 2023, arXiv:2210.01049, Phys. Rev. D, 108, 083522, Constraints on primordial non-Gaussianity from halo bias measured through CMB lensing cross-correlations
- [12] Atkins, Z., et al. 2023, arXiv:2303.04180, J. Cosmology Astropart. Phys., 2023, 073, The Atacama Cosmology Telescope: map-based noise simulations for DR6
- [13] Naess, S., et al. 2025, arXiv:2503.14451, arXiv e-prints, arXiv:2503.14451, The Atacama Cosmology Telescope: DR6 Maps
- [14] Storer, E. R. 2023, From Raw Data to Cosmology with the

¹⁷ https://github.com/simonsobs/tempura

¹⁸ https://github.com/simonsobs/falafel

¹⁹ https://github.com/simonsobs/so-lenspipe

²⁰ https://github.com/msyriac/orphics

- Atacama Cosmology Telescope, Ph.D. thesis, Princeton University (Princeton, NJ), http://arks.princeton.edu/ark:/88435/dsp01j3860b180
- [15] Dünner, R., et al. 2013, arXiv:1208.0050, ApJ, 762, 10, The Atacama Cosmology Telescope: Data Characterization and Mapmaking
- [16] Aiola, S., et al. 2020, arXiv:2007.07288, J. Cosmology Astropart. Phys., 2020, 047, The Atacama Cosmology Telescope: DR4 maps and cosmological parameters
- [17] Kim, J. & ACT Collaboration. in prep, The Atacama Cosmology Telescope: Measurement of the CMB lensing power spectrum from ACT+Planck over 27,000 sq. deg. and implications for structure formation
- [18] Abril-Cabezas, I. & ACT Collaboration. in prep, The Atacama Cosmology Telescope: LCDM Cosmological constraints from an ACT+Planck CMB lensing map over 27,000 sq. deg.
- [19] Qu, F. J. & ACT Collaboration. in prep, The Atacama Cosmology Telescope: Constraints on extensions to LCDM from an ACT+Planck CMB lensing map over 27,000 sq. deg.
- [20] Thornton, R. J., et al. 2016, arXiv:1605.06569, ApJS, 227, 21, The Atacama Cosmology Telescope: The Polarization-sensitive ACTPol Instrument
- [21] Louis, T., et al. 2025, arXiv:2503.14452, arXiv e-prints, arXiv:2503.14452, The Atacama Cosmology Telescope: DR6 Power Spectra, Likelihoods and ΛCDM Parameters
- [22] Abril-Cabezas, I., et al. 2025, arXiv:2505.03737, Phys. Rev. D, 112, 023522, Impact of Galactic non-Gaussian foregrounds on CMB lensing measurements
- [23] Madhavacheril, M. S., et al. 2020, arXiv:1911.05717, Phys. Rev. D, 102, 023534, Atacama Cosmology Telescope: Component-separated maps of CMB temperature and the thermal Sunyaev-Zel'dovich effect
- [24] Hilton, M., et al. 2021, arXiv:2009.11043, ApJS, 253, 3, The Atacama Cosmology Telescope: A Catalog of >4000 Sunyaev-Zel'dovich Galaxy Clusters
- [25] Duivenvoorden, A. J., et al. in prep, The Atacama Cosmology Telescope: beam measurements for DR6
- [26] Naess, S. & Louis, T. 2023, arXiv:2210.02243, The Open Journal of Astrophysics, 6, 21, Large-scale power loss in ground-based CMB mapmaking
- [27] Calabrese, E., et al. 2025, arXiv:2503.14454, arXiv e-prints, arXiv:2503.14454, The Atacama Cosmology Telescope: DR6 Constraints on Extended Cosmological Models
- [28] Maniyar, A. S., Ali-Haïmoud, Y., Carron, J., Lewis, A., & Madhavacheril, M. S. 2021, arXiv:2101.12193, Phys. Rev. D, 103, 083524, Quadratic estimators for CMB weak lensing
- [29] Namikawa, T., Hanson, D., & Takahashi, R. 2013, arXiv:1209.0091, MNRAS, 431, 609, Bias-hardened CMB lensing
- [30] Osborne, S. J., Hanson, D., & Doré, O. 2014, arXiv:1310.7547, J. Cosmology Astropart. Phys., 2014, 024, Extragalactic foreground contamination in temperature-based CMB lens reconstruction
- [31] Sailer, N., Schaan, E., & Ferraro, S. 2020, arXiv:2007.04325, Phys. Rev. D, 102, 063517, Lower bias, lower noise CMB lensing with foreground-hardened estimators
- [32] Sailer, N., Ferraro, S., & Schaan, E. 2023, arXiv:2211.03786, Phys. Rev. D, 107, 023504, Foreground-immune CMB lensing reconstruction with

- polarization
- [33] Planck Collaboration, et al. 2020, arXiv:1807.06210, A&A, 641, A8, Planck 2018 results. VIII. Gravitational lensing
- [34] Abdul Karim, M., et al. 2025, arXiv:2503.14739, Phys. Rev. D, 112, 083514, DESI DR2 results. I. Baryon acoustic oscillations from the Lyman alpha forest
- [35] Abdul Karim, M., et al. 2025, arXiv:2503.14738, Phys. Rev. D, 112, 083515, DESI DR2 results. II. Measurements of baryon acoustic oscillations and cosmological constraints
- [36] Simons Observatory Collaboration. 2019, arXiv:1808.07445, J. Cosmology Astropart. Phys., 2019, 056, The Simons Observatory: science goals and forecasts
- [37] Simons Observatory Collaboration. 2025, arXiv:2503.00636, J. Cosmology Astropart. Phys., 2025, 034, The Simons Observatory: science goals and forecasts for the enhanced Large Aperture Telescope
- [38] Prabhu, K., et al. 2024, arXiv:2403.17925, ApJ, 973, 4, Testing the ΛCDM Cosmological Model with Forthcoming Measurements of the Cosmic Microwave Background with SPT-3G
- [39] Astropy Collaboration. 2013, arXiv:1307.6212, A&A, 558, A33, Astropy: A community Python package for astronomy
- [40] Waltvan dervan der Walt, S., Colbert, S. C., & Varoquaux, G. 2011, arXiv:1102.1523, Computing in Science and Engineering, 13, 22, The NumPy Array: A Structure for Efficient Numerical Computation
- [41] Virtanen, P., et al. 2020, arXiv:1907.10121, Nature Methods, 17, 261, SciPy 1.0: fundamental algorithms for scientific computing in Python
- [42] Hunter, J. D. 2007, Computing in Science and Engineering, 9, 90, Matplotlib: A 2D Graphics Environment
- [43] Lewis, A., Challinor, A., & Lasenby, A. 2000, astroph/9911177, ApJ, 538, 473, Efficient Computation of Cosmic Microwave Background Anisotropies in Closed Friedmann-Robertson-Walker Models
- [44] Lewis, A. 2025, arXiv:1910.13970, J. Cosmology Astropart. Phys., 2025, 025, GetDist: a Python package for analysing Monte Carlo samples
- [45] Torrado, J. & Lewis, A. 2021, arXiv:2005.05290, J. Cosmology Astropart. Phys., 2021, 057, Cobaya: code for Bayesian analysis of hierarchical physical models
- [46] Zuntz, J., et al. 2015, arXiv:1409.3409, Astronomy and Computing, 12, 45, CosmoSIS: Modular cosmological parameter estimation
- [47] Planck Collaboration, et al. 2016, arXiv:1502.01588, A&A, 594, A10, Planck 2015 results. X. Diffuse component separation: Foreground maps
- [48] Song, Y.-S., Cooray, A., Knox, L., & Zaldarriaga, M. 2003, astro-ph/0209001, ApJ, 590, 664, The Far-Infrared Background Correlation with Cosmic Microwave Background Lensing
- [49] Cooke, R. J., Pettini, M., & Steidel, C. C. 2018, arXiv:1710.11129, ApJ, 855, 102, One Percent Determination of the Primordial Deuterium Abundance
- [50] Mossa, V., et al. 2020, Nature, 587, 210, The baryon density of the Universe from an improved rate of deuterium burning

End Matter

TABLE II. Summary of PTE values inferred from the different map-level null tests, where the reconstruction was performed with the MV estimator. They show no evidence of an additive systematic in the daytime maps.

Map-level null test	Day deep	Daywide	Daytime
coadd	0.97	0.51	0.97
$90\mathrm{GHz}$	0.77	0.88	0.77
$150\mathrm{GHz}$	0.54	0.10	0.50
PA5	0.78	0.87	0.86
PA6	0.89	-	_

Summary of null tests—We summarize in Tables II–IV the PTEs of all null tests derived using the MV estimator. For each category, we run both all frequency-coadded arrays (row labeled "coadd") and subsets of those: single polarized arrays (PA5, PA6) and single frequencies (90 GHz and 150 GHz). Except for the multipole-range stability tests, we always compare nighttime to daytime data. We obtain the reconstructions on both daydeep and daywide data (second and third columns). then sum the resulting bandpowers with inverse variance weighting and a covariance derived from simulations to obtain the final daytime bandpowers (last column, labeled "Daytime"). Table II summarizes the results corresponding to the map-level null tests. They show no evidence of an additive systematic in the daytime maps. Table III reports the PTEs for the corresponding bandpower-level null tests. We find just one marginal failure, when we compare the daywide and nighttime 150 GHz bandpowers.

We also test for consistency between our baseline bandpowers and those obtained when including a less extended range of CMB modes. These are reported in the five bottom rows of Table III. We only find a marginal failure when varying $\ell_{\rm min}$ in daywide (PTE value of 0.020 in the 800 < $\ell_{\rm CMB}$ < 3000 test). This is most likely related to the 150 GHz marginal failure in this same dataset, and it only affects temperature. When we check for stability using only $\ell_{\rm CMB} > 1000$ modes in polarization (sixth row), we find good agreement with our baseline bandpowers. The latter test ensures that the inclusion of a transfer function within the polarization effective beam, which should really only be present in temperature, is not biasing our results in any significant way.

Finally, we ensure that we detect no curl in the CMB lensing reconstructions above. These are reported in Table IV. Even though the PTE distribution (see lower panel of Fig. 5) is consistent with uniform, the PTEs are a bit skewed towards low values. However, if not due to a fluctuation, this may be due to the errors being slightly underestimated, instead of a systematic in the data: we

TABLE III. Summary of PTE values derived from the different bandpower-level null tests. Overall, we find good agreement between the nighttime and daytime bandpowers. We also check that the daytime reconstructed bandpowers are stable with respect to using a more restricted range of CMB modes. See text for more details regarding the two marginal failures (highlighted in bold).

Bandpower-level null test	Day deep	Daywide	Daytime
coadd	0.72	0.42	0.41
$90\mathrm{GHz}$	0.84	0.24	0.45
$150\mathrm{GHz}$	0.35	0.015	0.60
PA5	0.41	0.41	0.20
PA6	0.61	_	_
$\ell_{\rm min}({ m pol})~1000$	0.40	0.65	0.41
$1000 < \ell_{\rm CMB} < 3000$	0.47	0.12	0.96
$800 < \ell_{\rm CMB} < 3000$	0.94	0.020	0.41
$600 < \ell_{\rm CMB} < 2000$	0.51	0.12	0.27
$600 < \ell_{\rm CMB} < 2500$	0.64	0.75	0.83

TABLE IV. PTE values for the different bandpower-level curl null tests. The curl of the reconstructed lensing deflection field is expected to be zero at these noise levels. The distribution of PTE values, shown in the lower panel of Fig. 5, is consistent with a uniform distribution (Kolmogorov–Smirnov test PTE of 9%, with the caveat that this test ignores correlations between the different tests).

Bandpower-level null test	Day deep	Daywide	Daytime
coadd	0.33	0.22	0.41
$90\mathrm{GHz}$	0.41	0.61	0.79
$150\mathrm{GHz}$	0.34	0.25	0.22
PA5	0.39	0.22^{a}	0.20
PA6	0.17	_	0.17^{b}

^a The *daywide* result for PA5 (curl) is the same as all array-bands coadded ("coadd"), since this dataset does not include PA6. We do not double count this result in the histogram compilation.

checked every test individually and found no worrisome shape.

Mapping the dark matter distribution during the day—We show in Fig. 7 the reconstructed projected matter density field in the southern daydeep region. The white regions correspond to peaks in the matter density field, while the dark regions correspond to voids. One can see by eye the correspondence between the mass map and the Cosmic Infrared Background (CIB) measured by Planck [47], overlaid in contours (where blue and red correspond to underdensities and overdensities, respectively). These two fields are in fact expected to be highly correlated [48].

Daytime lensing bandpowers—Complementary to

b The "Daytime" result for PA6 (curl) is that of daydeep PA6 (curl). This is only counted once in the histogram compilation.

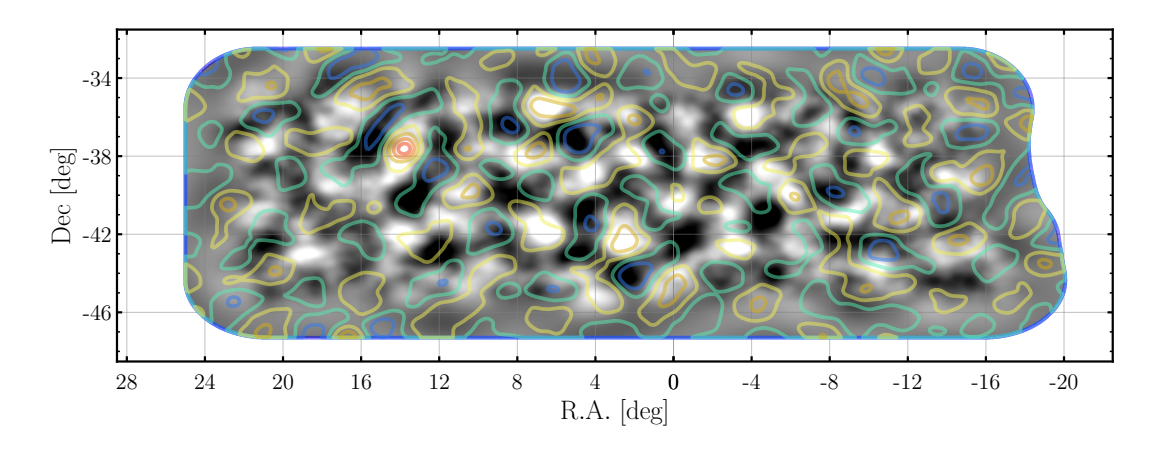


FIG. 7. Wiener-filtered map of the reconstructed projected matter density field in the southern daydeep region (grayscale). Overlaid is a map of the CIB as measured by Planck at 545 GHz [47] (underdensities in blue, overdensities in red). Both signals should be highly correlated, based on their similar $z \sim 2$ origin [48]. Indeed, one can see by eye the correspondence between the two fields.

TABLE V. ACT DR6 daytime CMB lensing bandpowers $\hat{C}_L^{\kappa\kappa}$. The multipole bin edges $[L_{\min}, L_{\max}]$ are given in the first column and the band centers L_b in the second.

$\overline{[L_{\min}, L_{\max}]}$	L_b	$10^7 \hat{C}_L^{\kappa\kappa}$
[40, 66]	53.0	2.23 ± 0.37
[67, 101]	83.5	2.11 ± 0.26
[102, 145]	123.0	1.42 ± 0.18
[146, 199]	172.0	1.18 ± 0.14
[200, 264]	231.5	0.63 ± 0.13
[265, 339]	301.5	0.67 ± 0.13
[340, 426]	382.5	0.40 ± 0.11
[427, 526]	476.0	0.284 ± 0.085
[527, 638]	582.0	0.201 ± 0.077
[639, 763]	700.5	0.118 ± 0.071

TABLE VI. Priors used to obtain the cosmological constraints presented in this work. Uniform priors are shown in square brackets and Gaussian priors with mean μ and standard deviation σ are denoted $\mathcal{N}(\mu, \sigma)$.

Parameter	Prior
$\ln(10^{10}A_s)$	[2, 4]
$H_0[{\rm kms^{-1}Mpc^{-1}}]$	[40, 100]
n_s	$\mathcal{N}(0.96, 0.02)$
$\Omega_b h^2$	$\mathcal{N}(0.0223, 0.0005)$
$\Omega_c h^2$	[0.005, 0.99]
au	0.055 (fixed)

Fig. 6, Table V reports the ACT DR6 day time CMB lensing bandpowers $\hat{C}_L^{\kappa\kappa}.^{21}$

Likelihood— We use a Gaussian likelihood \mathcal{L} to obtain

FIG. 8. Variance of the reconstruction noise per-mode for the *daydeep* (orange), *daywide* (blue) and night (yellow) ACT DR6 datasets, in comparison to the fiducial P-ACT lensing power spectrum prediction (shown in black).

constraints on cosmological parameters:²²

$$-2\ln\mathcal{L} \propto \sum_{bb'} \left[\hat{C}_{L_b}^{\kappa\kappa} - C_{L_b}^{\kappa\kappa}(\boldsymbol{\theta}) \right] \mathbb{C}_{bb'}^{-1} \left[\hat{C}_{L_{b'}}^{\kappa\kappa} - C_{L_{b'}}^{\kappa\kappa}(\boldsymbol{\theta}) \right], (2)$$

where $C_{L_b}^{\kappa\kappa}(\boldsymbol{\theta})$ is the theory lensing spectrum for a given cosmological parameter combination $\boldsymbol{\theta}$, and $\mathbb{C}_{bb'}$ is the covariance matrix. We summarize our choice of priors in Table VI. These are consistent with previous lensing analyses [2–4, 33]. CMB lensing is not sensitive to the CMB optical depth (as we probe the total matter power spectrum), so it is fixed to $\tau=0.055$. The prior on $\Omega_b h^2$ is informed by the Big Bang

Daydeep — Daywide — Night

4

101

102

103

L

 $^{^{21}}$ The associated covariance $\mathbb C$ is available at https://github.com/ACTCollaboration/dr6plus_lenslike.

²² The likelihood is publicly available at https://github.com/ ACTCollaboration/dr6plus_lenslike.

nucleosynthesis prediction that matches the primordial deuterium abundance measurement [49, 50].

Per-mode reconstruction noise—We show in Fig. 8 the noise power spectra for the ACT dr6.02 datasets. Both night and daydeep are signal-dominated on scales $L\lesssim 150.$ While the daydeep maps have a greater depth,

they only cover a fifteenth of the night's area. *Daywide* has a reconstruction noise power more than three times larger than the other two datasets. We defer a detailed discussion of the relative contributions of daytime and nighttime data to the final lensing power spectrum to the upcoming ACT DR6+ lensing papers [17–19].